

Evolution of Creep Damage of 316L Produced by Laser Powder Bed Fusion

Alexander Ulbricht,* Luis Alexander Ávila Calderón, Konstantin Sommer, Gunther Mohr, Alexander Evans, Birgit Skrotzki, and Giovanni Bruno

The damage mechanisms of metallic components produced by process laser powder bed fusion differ significantly from those typically observed in conventionally manufactured variants of the same alloy. This is due to the unique microstructures of additively manufactured materials. Herein, the focus is on the study of the evolution of creep damage in stainless steel 316L specimens produced by laser powder bed fusion. X-ray computed tomography is used to unravel the influence of the process-specific microstructure from the influence of the initial void distribution on creep damage mechanisms. The void distribution of two specimens tested at 600 °C and 650 °C is analyzed before a creep test, after an interruption, and after fracture. The results indicate that the formation of damage is not connected to the initial void distribution. Instead, damage accumulation at grain boundaries resulting from intergranular cracking is observed.

components produced by PBF-LB/M is the freedom of design, which enables material reduction to the minimum required to withstand the expected loads.^[3,4] This contrasts to conventionally produced components (such as castings, millings, or forged) which are limited by the constraints of machining capability.^[5,6] Nonetheless, this surplus material adds to the safety margin of these parts.^[7] PBF-LB/M parts might not possess this intrinsic additional safety margin. This apparent dilemma generates a stronger need for understanding how PBF-LB/M components respond to the application of external loads. This knowledge is especially needed for the engineering design of PBF-LB/M components to be used in safety critical environments and applications.

1. Introduction


Over the last decade, additive manufacturing (AM) of metals has evolved from a rapid prototyping technique to a mature industrial production process with applications in several industries, even in aerospace.^[1] Among the AM production processes, laser powder bed fusion (PBF-LB/M; this abbreviation of powder bed fusion using a laser beam of metallic feedstock material follows the nomenclature defined in DIN EN ISO/ASTM 52900-21 and replaces the abbreviation LPBF^[2]) has become relevant since it enables the production of net-shape metallic parts that do not need additional machining.^[3] One aim of PBF-LB/M is the reduction of the amount of necessary material to produce light-weight components. In fact, the main advantage of metallic

One of the most commonly used alloys in industry is stainless steel AISI 316L, thanks to its high corrosion resistance and good processing properties.^[8,9] The use of PBF-LB/M/316L starts to become relevant for industrial applications.^[10] In order to implement the material's use in high temperature environments and safety critical applications, a profound knowledge of the properties of PBF-LB/M/316L is required.

Despite the increasing use of PBF-LB/M/316L in industry, literature on the evolution of damage—especially of creep—in this material is still limited.^[11–15] Ávila et al.^[11] had shown that the damage mechanisms in PBF-LB/M/316L differ significantly from the mechanisms in conventionally produced 316L. They suggested that PBF-LB/M/316L accommodates external creep strains presumably during tertiary creep by creating micro-cracks along the grain boundaries instead of undergoing plastic deformation. Yoon et al. demonstrated the occurrence of cracking at grain boundaries in their PBF-LB/M/316L specimens.^[12] Williams et al. reported for PBF-LB/M/316L, where the loading axis was parallel to the build direction, large transgranular cracks and intergranular creep micro-cracks apparently starting mainly from lack of fusion defects and, to a lesser extent, gas porosity.^[13] The intergranular micro-cracks were considered to be a product of coalescence of creep cavities at grain boundaries and were observed at grain boundaries, both perpendicular and nearly parallel to the building direction. The ultimate fracture was due to the branching and linking of the micro-cracks through multiple defects and across multiple layers. Such fracture was transgranular in nature. The material studied had a defect volume fraction smaller than 0.5%. In the work of Li et al. on PBF-LB/M/316L, grain boundary cracking was the predominant failure mode.^[14]

A. Ulbricht, L. A. Ávila Calderón, K. Sommer, G. Mohr, A. Evans, B. Skrotzki, G. Bruno
Bundesanstalt für Materialforschung und -prüfung (BAM)
Unter den Eichen 87, 12205 Berlin, Germany
E-mail: alexander.ulbricht@bam.de

G. Bruno
Institute of Physics and Astronomy
University of Potsdam
Karl-Liebknecht-Straße 24/25, 14476 Potsdam, Germany

 The ORCID identification number(s) for the author(s) of this article can be found under <https://doi.org/10.1002/adem.202201581>.

© 2023 The Authors. Advanced Engineering Materials published by Wiley-VCH GmbH. This is an open access article under the terms of the Creative Commons Attribution License, which permits use, distribution and reproduction in any medium, provided the original work is properly cited.

DOI: 10.1002/adem.202201581

The grains were highly elongated, and the cracks mainly grew along the grain boundaries perpendicular to the loading direction. Some large cracks mixed with a high density of microcracks along the grain boundaries were observed. The volume fraction of defects in the studied region was 0.10%, being higher and more concentrated toward the center (0.18%). As shown in previous studies of PBF-LB/M/316L, the process parameters used define the characteristics of the microstructure.^[16,17] It had been presented in literature that the characteristics of a polycrystalline material microstructure affects strongly its material properties in terms of deformation and damage evolution.^[18] Therefore, conclusions regarding service life of PBF-LB/M/316L could only be drawn for the specifically studied microstructure.

This study follows the work of Ávila et al.^[11] The same simple bidirectional scanning strategy with 90° rotation from layer to layer was used during PBF-LB/M/316L specimen production. Such scanning strategy results in columnar grain morphology. This specific grain morphology enables easy recognition of intergranular cracks since the latter appear in a similar fashion. This study focusses on a more detailed analysis of PBF-LB/M/316L's response to creep loading in terms of damage accumulation by using X-ray micro computed tomography (XCT) than in the previous study by Ávila et al.^[11] In addition to the microscopy analysis of broken creep specimens, the evolution of void formation is nondestructively analyzed using XCT before the creep test, after an interruption, and after failure. XCT analysis enables the non-destructive analysis of specimens' microstructural features and defects (void population) in the complete volume. Therefore, patterns of internal creep damage could be easily recognized than with 2D methods such as metallographic sections.

Williams et al. have studied PBF-LB/M/316L creep specimens, but they used a different scan strategy and used a pulsed laser (therefore, producing a different microstructure).^[13] They reported that the size, shape, and location of the initial voids had a larger influence on rupture life than the applied stress.

In this study, we aimed to track the positions of the initial voids through the creep test. Therefore, the same XCT analysis as performed prior to creep testing was repeated during a defined interruption of the creep test at the start of tertiary creep. Finally, the two specimens were analyzed after fracture. By this multi-stage procedure, the material's response to creep loading in terms of damage evolution with respect to initial porosity could be shown.

2. Experimental Section

2.1. Specimen Production

Two creep specimens tested at different temperatures and creep loads were analyzed by XCT at three stages of creep testing. The inherent initial porosity of PBF-LB/M/316L specimens as well as their spatial distribution were analyzed prior to the mechanical tests to study their influence on the evolution of creep damage. The PBF-LB/M/316L creep specimens were produced in-house using a SLM280HL (SLM Solutions Group AG, Lübeck, Germany). The machine is equipped with a 400 W continuous wave ytterbium fiber laser. It has a focal spot size of 80 µm at

an emitted wavelength of 1070 nm.^[11,19] Argon was used as shielding gas during the production of the specimens. The feedstock 316L powder was characterized by its supplier. Details on powder characterization are given in the paper by Ávila et al.^[11] The following process parameters were used to produce the specimens: a laser power of 275 W, a scan velocity of 700 mm s⁻¹, a hatch distance of 0.12 mm, a layer thickness of 0.05 mm, and an inter-layer time of approx. 65 s. A bidirectional scanning strategy was applied which alternated the scanning vectors' orientation by 90° between odd and even layers. Prisms with dimensions (20 × 13 × 114,5) mm³ were produced. The prisms were heat treated at 450 °C for 4 h to relieve internal stresses. From the prisms, cylindrical creep specimens with dimensions 100 mm × M12 were machined to prevent surface roughness from influencing the creep test results. Further details are described by Ávila et al. and Charmi et al.^[11,20]

2.2. Creep Testing

Creep testing was performed in-house according to DIN EN ISO 204:2019-04, i.e., with constant force until rupture (see Ávila et al. for further details of the mechanical test).^[11,21] The loading direction of the creep tests coincided with the build direction of the creep specimens. Two PBF-LB/M/316L creep specimens were tested under different test conditions: One specimen was tested at 600 °C/200 MPa and the other at 650 °C/175 MPa. The creep tests were interrupted to enable XCT inspection at a specific time for each specimen approx. at the first quarter of the tertiary creep phase. To interrupt the tests, the specimens were cooled down to room temperature and unloaded afterward. The time of interruption t_i is marked in the creep curves given in **Figure 1** and in **Table 1**. Besides, Table 1 shows that the percentage plastic extension e_p of both specimens consists only of the percentage creep extension e_f . The total plastic strains at the point of interruption were 0.39% for the 600 °C/200 MPa creep specimen and 0.53% for the 650 °C/175 MPa creep specimen. Most of the percentage plastic/creep extension was developed during the test period after the interruption, as visible in **Figure 1**. The

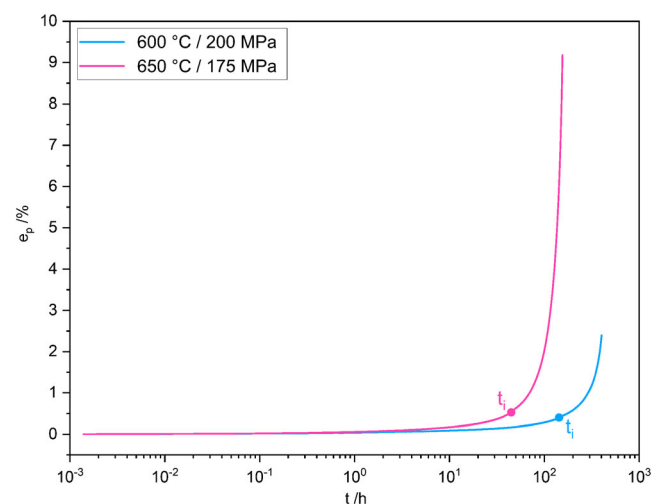


Figure 1. Creep curves e_p versus t of the two tested specimens including the interruption time t_i .

Table 1. Experimental data of the creep tests of the PBF-LB/M/316 L creep specimens as presented in the paper of Ávila et al.^[11]

Testing temperature	Initial stress	Creep rupture time	Time of interruption	Percentage initial total extension	Percentage elastic extension	Percentage initial plastic extension	Percentage creep extension	Percentage plastic extension
T [°C]	R_0 [MPa]	t_u [h]	t_i [h]	e_{ti} [%]	e_e [%]	e_i [%]	e_f [%]	e_p [%]
600	200	402	143	0.19	0.19	0.00	2.40	2.40
650	175	155	44.8	0.18	0.18	0.00	9.20	9.20

extensions showed in Table 1 are related to each other according to Equation (1)–(3). The term e_t represents the total extension. All other extension components are listed in Table 1

$$e_t = e_{ti} + e_f \quad (1)$$

$$e_{ti} = e_e + e_i \quad (2)$$

$$e_p = e_t - e_e = e_i + e_f \quad (3)$$

2.3. Micro Computed Tomography

Both creep specimens were analyzed by XCT in the three stages of the creep experiment. The XCT data acquisition of the specimens before testing and after the first interruption of the creep test was performed on a GE v|tome|x 180/300 commercial XCT scanner (GE Sensing and Inspection GmbH, Wunstorf, Germany). The CT scan after the interruption was performed without the application of external load. So, existing cracks, which lips were closed during unloading, cannot be detected because closed cracks do not change the local X-ray absorption. The used scan parameters are given in Table 2. The XCT scan of the specimens after rupture was performed using a custom built XCT scanner. The used scan parameters are given in Table 3. To achieve a voxel size of 10 μm , the specimens had to be scanned at different heights. The reconstructed data of each height were stitched to create a 3D volume of the whole specimen. Subtle variations in the gray-level distribution are visible in the merged 3D volume of the broken specimens. The reconstructed data of all XCT scans were filtered using the filter nonlocal means

Table 2. XCT acquisition parameters for the two creep specimens before the test and after the interruption.

Voltage [kV]	Current [μA]	Projections			Filter [mm]	Voxel size [μm]
		N _p	Time [s]	Average		
200	50	2600	2	–	Ag 0.25	10

Table 3. XCT acquisition parameters for the two broken specimens.

Voltage [kV]	Current [μA]	Projections			Filter [mm]	Voxel size [μm]
		N _p	Time [s]	Average		
210	70	2100–2250 ^{a)}	2	5	Cu 1.0 Al 0.25	10

^{a)}The number of needed projections differed slightly for the broken parts due to alignment.

denoising of the open-source imaging software Fiji to reduce the noise in the data.^[22–24] Segmentation of internal structures in the reconstructed data was performed using the commercial 3D image analysis software VG Studio MAX version 3.3 (Volume Graphics GmbH, Heidelberg, Germany) and the open-source software iLastik.^[25] A lower threshold of 8 voxels was used to define voids.

2.4. Optical Microscopy

The microstructure of the PBF-LB/M/316L specimens of this study was characterized by optical microscopy on twin specimens built with the same process parameters and on the same PBF-LB/M machine. These specimens were ground to the plane of analysis as well as polished and etched. The preparation and image acquisition process are described in detail by Ávila et al.^[11]

3. Results

The initial porosity of the two creep specimens was very low ($<0.01\%$). This was in agreement to previous studies of the same material produced by PBF-LB/M/316L.^[21] In the two specimens a sparse population of spherical voids was found (see Figure 2a and 3a). Their average equivalent diameter was 29 μm .

In the XCT data acquired after the interrupted creep test, additional voids were found in both specimens. Still, the total porosity remained below 0.01%. A slight change in the aspect ratio of the initial voids (i.e., elongation) in the loading direction was observed (see Figure 4). No micro-cracking could be detected in the XCT reconstructions.

A large increase in the number of detected voids was observed along the whole length of both specimens after rupture. In both specimens, the highest density of voids was detected near the rupture surface. Due to the slight gray level variation in the 3D reconstructed volumes, some artefacts were observed at the locations of the stitches. These stitching artefacts influence the quality of the segmentation of voids. Therefore, the void distribution in Figure 2c and 3c could be analyzed in a qualitative fashion.

The XCT data of both broken specimens revealed a network of voids (see Figure 2 and 3). The spatial distribution of these voids was arranged in a grid. Its shape and size resemble the grain morphology of the PBF-LB/M/316L material. Due to the amount of creep-induced damage (overlapping myriad of further defects) and the elongation of the specimens, it was not possible to retrace the location of the individual initial voids in the broken specimens. In the 650 °C/175 MPa creep specimen (Figure 3), creep-induced voids occur throughout the whole specimen's length. Their spatial density increases toward the location of the rupture.

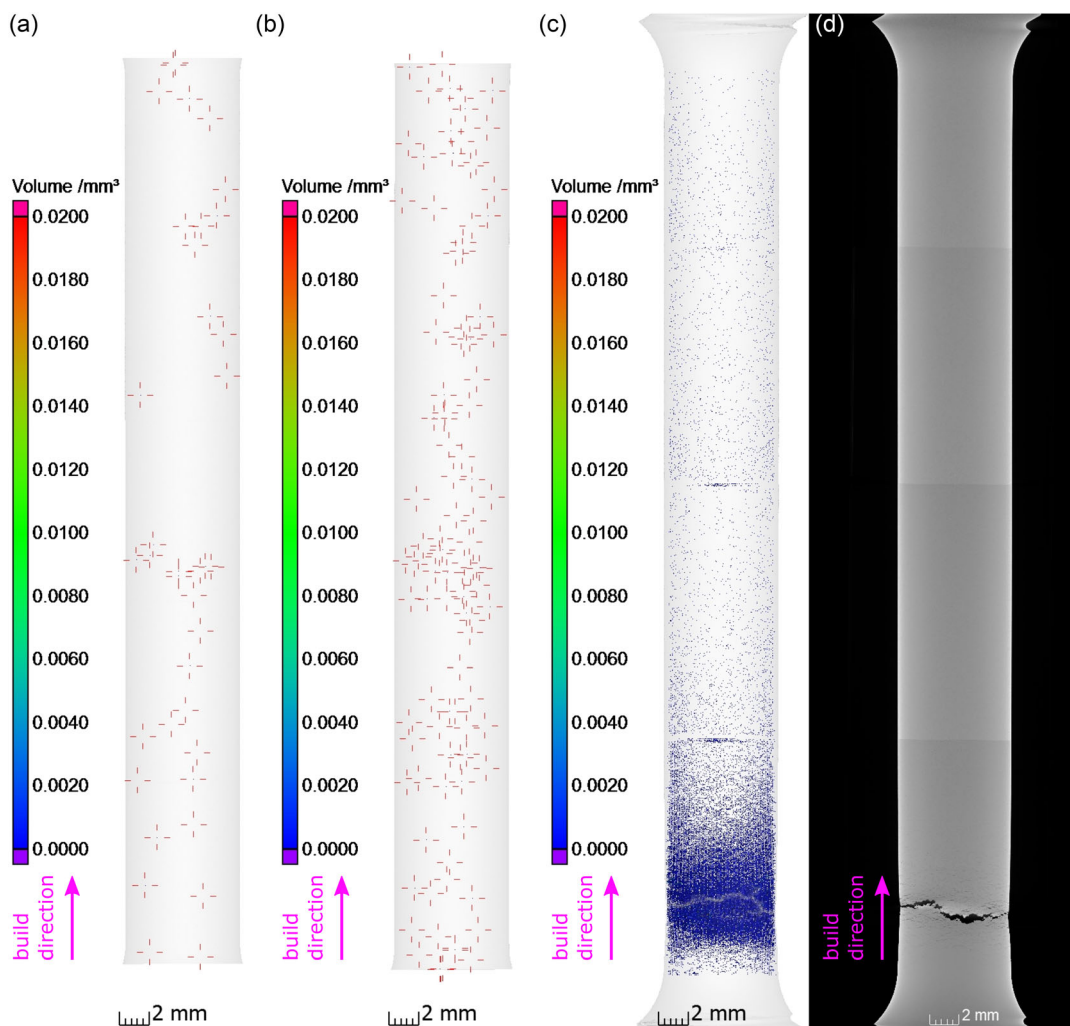


Figure 2. XCT reconstruction of the 600 °C/200 MPa specimen at different stages of the creep test: a) Void distribution before the creep test; b) void distribution after test interruption; c) void distribution after rupture; d) virtual cut at the maximum specimen vertical cross section.

In comparison, in the 600 °C/200 MPa specimen (Figure 2), creep-induced voids are more sparsely distributed through the overall length of the specimen, and their distribution density sharply increases near the rupture surface. A comparison of the material's microstructure and segmented voids reveals a correlation between the shape of the segmented voids and the grain morphology (see Figure 5). As shown in the figure, voids are primarily formed by cracking at grain boundaries oriented nearly perpendicular to the build direction (from now on referred to as "horizontal grain boundaries"). The figure also shows that connected microcracks form clusters (the largest connected micro-crack in Figure 5b is highlighted in red). Grain boundaries oriented parallel to the build direction (from now on referred to as "vertical grain boundaries") remain broadly intact, unless isolated networks of micro-cracks are formed, as observed on the final fracture surface. These features have also been observed by optical microscopy.^[11]

For completeness, Figure 6 shows optical microscopy images of the damage characteristics. The micrograph before etching,

Figure 6a, is shown as reference. There, the melt pool boundaries are not visible. The etched surface (see figure 6b), which reveals both the grain boundaries and, in less strong contrast, the melt pool boundaries, shows that the micro-cracks form at the horizontal grain boundaries. The figure also reveals that the rupture surface is formed by a network of micro-cracks along those grain boundaries. Additionally, three melt pool boundaries are highlighted in red to emphasize the fact that micro cracks form along horizontal grain boundaries rather than along melt pool boundaries. An inspection of the rupture surfaces revealed a checkerboard-like structure, which matches the spatial distribution of the voids found in the two specimens (see Figure 7).

The broken parts of each of the two specimens were virtually matched in VG Studio MAX in such a way that the outer circumferences of both parts were matched without leaving a gap. However, a small gap in the center between the two parts was observed (see Figure 8).

A major difference was observed between the two specimens (see Table 4) when determining the total length of the matched

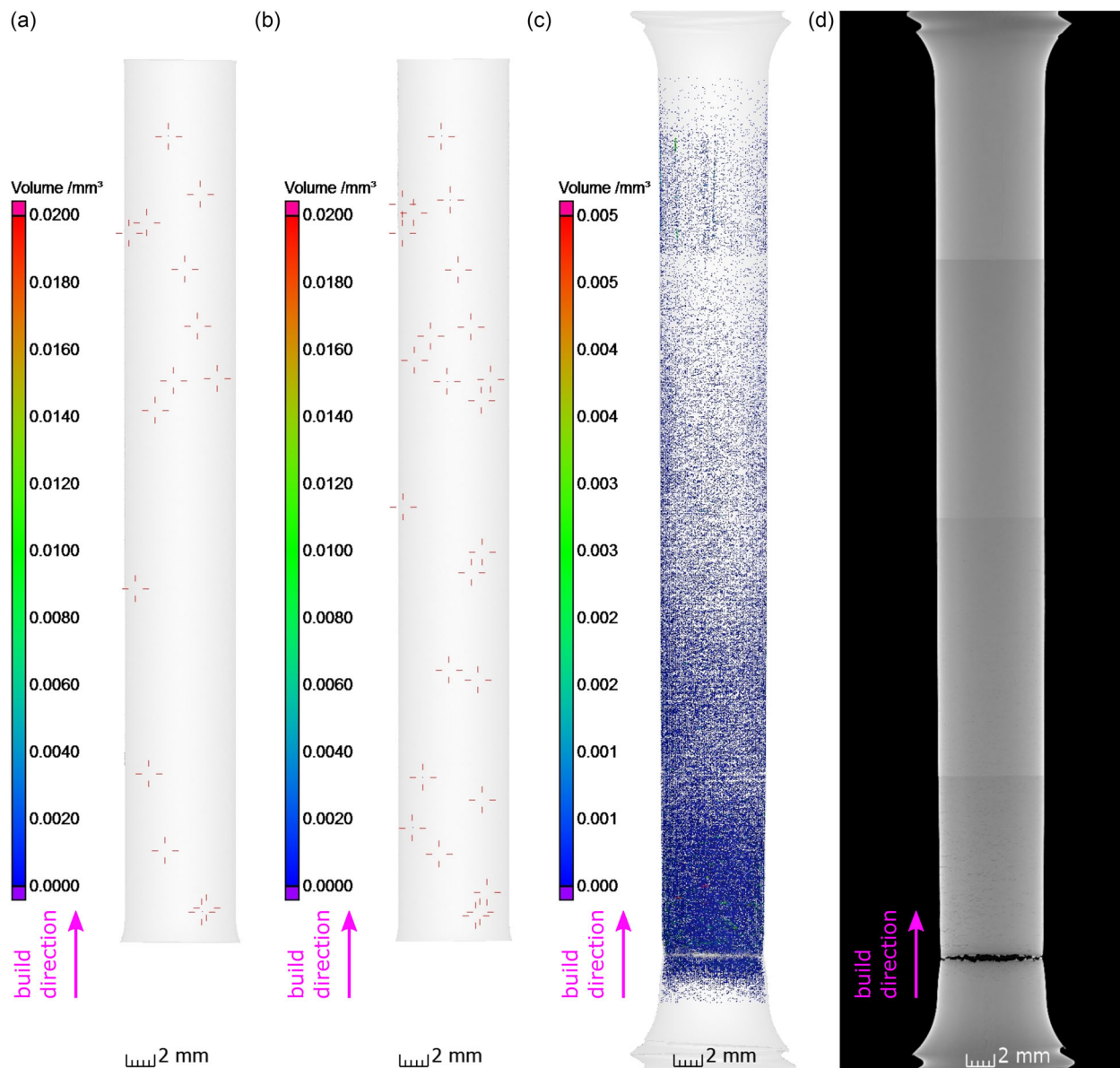


Figure 3. XCT reconstruction of the 650 °C/175 MPa specimen at different stages of the creep test: a) Void distribution before the creep test; b) void distribution after test interruption; c) void distribution after rupture; d) virtual cut at the maximum specimen vertical cross section.

parts from the XCT data. The merged broken parts of the 600 °C/200 MPa specimen revealed a total elongation of only about 1.2 mm. For the 650 °C/175 MPa specimen an elongation of about 5.5 mm was observed. This observation is consistent with the larger plastic extension e_p of the 650 °C/175 MPa specimen in comparison to the 600 °C/200 MPa specimen, as shown in Table 1.

4. Discussion

As shown by Ávila et al., the same batch of PBF-LB/M/316L exhibited lower creep ductility than conventionally manufactured 316L.^[11] Comparisons to conventionally manufactured creep

specimens in this study are based on their results. Therefore, the authors refer to Ávila et al. for a detailed discussion on the differences between the studies PBF-LB/M/316L and conventionally manufactured 316L.^[11] The creep behavior of the studied PBF-LB/M/316L is characterized by a less pronounced reduction of the cross section area, lower creep extension, and lower total elongation compared to the conventionally manufactured 316L.^[11] Ávila et al. showed that cracking at grain boundaries is the dominant damage formation mechanism for this specific PBF-LB/M/316L material.^[11] Also Li et al. reported intergranular cracking for their PBF-LB/M/316L creep specimens.^[26] Intergranular cracking had also been reported for heat treated creep specimens of other PBF-LB/M materials, such as IN718.^[27,28] For conventionally manufactured 316L, the degree

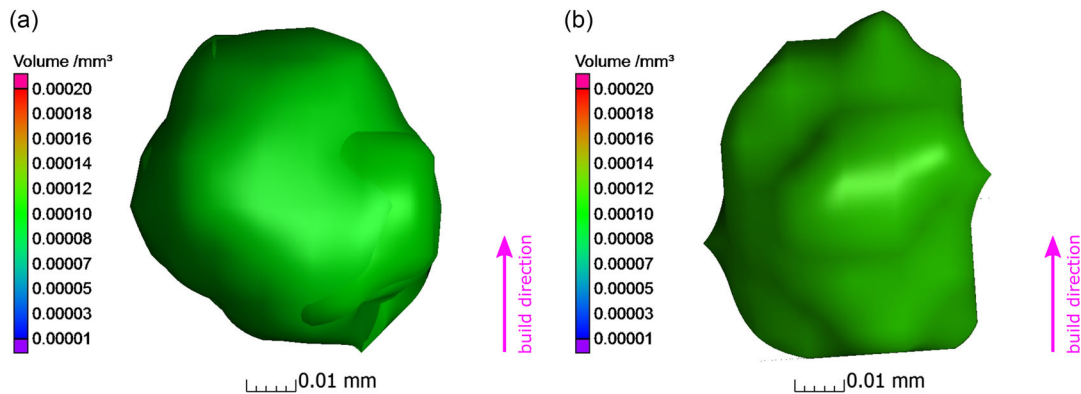


Figure 4. 3D rendering of the largest void found in the 600 °C/200 MPa specimen: a) before the creep test; b) after interruption.

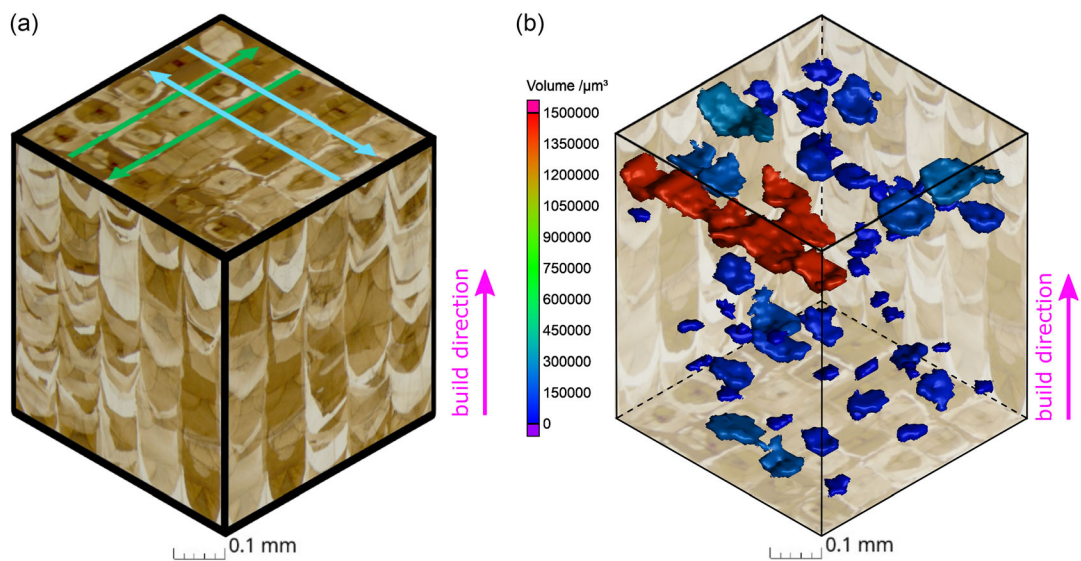


Figure 5. Comparison of the microstructure of the PBF-LB/M/316L material and the shape of the segmented micro-cracks after fracture: a) Generic volume element obtained from microscopy images of the same batch of PBF-LB/M/316L material: alternating bidirectional scan orientations for odd and even layers are marked in green and blue; build direction is marked in pink; b) combination of the segmented damaged section of the 650 °C/175 MPa specimen and the microscopy images at the same scale.

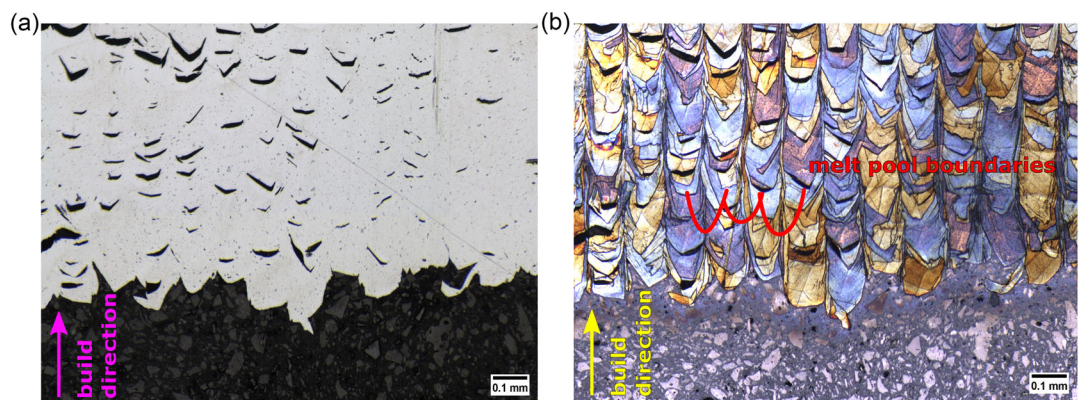


Figure 6. Optical microscopy images of a cut section of the 650 °C/175 MPa specimen. The longer upper part of the broken specimen was cut along the build direction: a) Before etching and b) the very same section after etching. Three melt pool boundaries are highlighted in red.

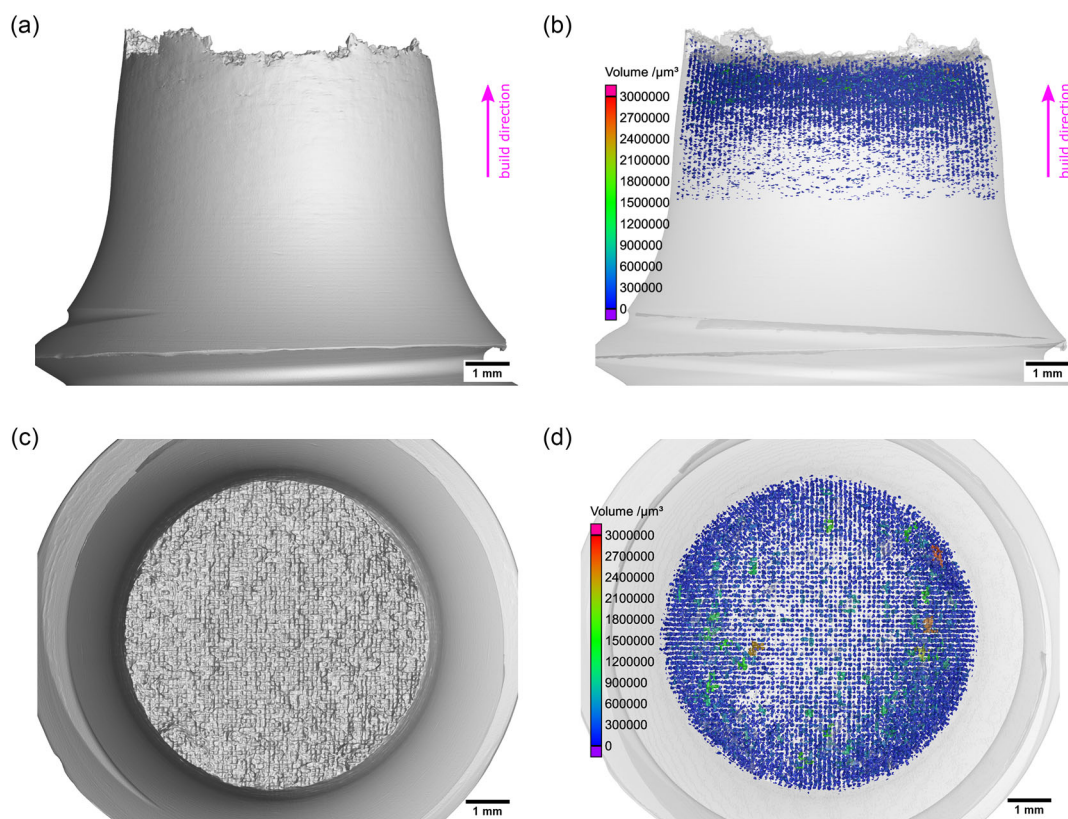


Figure 7. 3D rendering of the bottom part's top view of the 650 °C/175 MPa specimen: a) rendering of the rupture surface—side view; b) rendering of the void distribution—side view; c) rendering of the rupture surface—top view; d) rendering of the void distribution—top view.

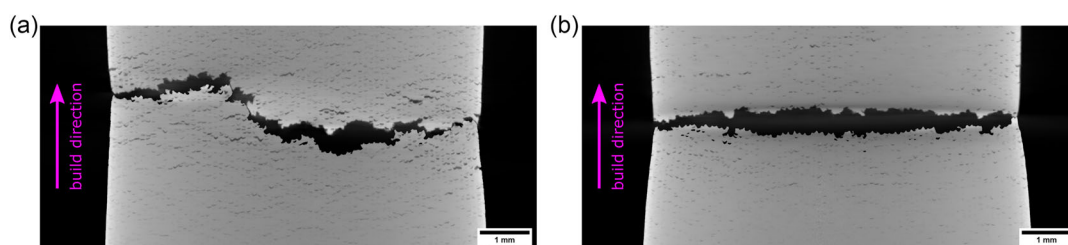


Figure 8. Gap between the centers of the two broken parts after combination: a) 600 °C/200 MPa specimen; b) 650 °C/175 MPa specimen.

Table 4. Parallel length of the specimen obtained from XCT results.

Testing condition of the specimens	Point of time for XCT scan		
	t_0 [mm]	t_i [mm]	t_u [mm]
600 °C/200 MPa	(60.2 ± 0.5)	(60.4 ± 0.5)	(61.7 ± 0.5)
650 °C/175 MPa	(60.1 ± 0.5)	(60.4 ± 0.5)	(65.6 ± 0.5)

of intergranular damage as shown by XCT and optical microscopy is significantly lower for the same testing conditions.^[11] Previous studies on conventionally manufactured 316 L have shown that intergranular cracking can occur at testing conditions above 600 °C/275 MPa and 625 °C/ \approx 230 MPa.^[29,30] This behavior indicates that intergranular damage is inherent to 316L at such testing conditions. However, the study by Ávila et al.

highlights that the degree of intergranular cracking appears greater for PBF-LB/M/316L than for conventionally manufactured 316L at the tested conditions. The XCT analysis results reported in this work on the two inspected PBF-LB/M/316L specimens fully corroborate the results shown by Ávila et al.^[11] In Section 2.2, it was mentioned that most of the plastic/creep extension observable by XCT seems to develop after the interruption of the test period. The results presented in Section 3 (Figure 2 and 3) indicate that most of the creep damage develops during that time frame as well. During the interruption only changes in the aspect ratio of initial pores could be detected by XCT (i.e., voids subtle elongated along the loading direction). Optical microscopy images of metallographic cuts of the broken specimens did not indicate other damage mechanisms than the reported micro-cracking at horizontal grain boundaries.

The absence of micro-cracks in the XCT data on both specimens after creep test interruption (i.e., at the end of the secondary stage of creep) could lead to the conclusion that either micro-cracking occurs in late stages of creep (tertiary) or that the lips of already existing micro-cracks could either be closed because of the load release (interruption) or below the resolution of the XCT. Closed micro-crack lips cannot be detected by XCT since they do not cause any change to the X-ray absorption. Only open cracks can be detected since voids air between the lips lead to changes in the X-ray absorption.

The XCT results reveal that the emergence of micro-cracks in the PBF-LB/M/316L seems to be the key mechanism causing the creep deformation. The higher accumulation of damage of 650 °C/175 MPa than in the 600 °C/200 MPa specimen well corresponds to the almost four times larger creep extensions observed. The shape of these micro-cracks resembles the grain morphology of the material. From their size and shape, it can be deduced that these micro-cracks primarily formed at the horizontal grain boundaries, as also shown by Ávila et al.^[11] We showed in this work that these micro-cracks can form clusters. In agreement with Li et al., the XCT analysis of the rupture surface also revealed that it is mainly formed by a network of intergranular micro-cracks of horizontal (i.e., perpendicular to the load axis) grain boundaries.^[26] Throughout both specimens, the areas near the vertical grain boundaries are less affected by cracking (the void-free sections between the defect columns). Near the rupture surface, some necking could be observed (see Figure 7), but not to the extent shown by conventional hot rolled 316 L, where creep leads to a significant reduction of area.^[11] This indicates that the rupture was a combination of intergranular cracking of the horizontal grain boundaries and ductile fracture (plastic deformation in regions of predominantly vertical grain boundaries). A small gap remained after stitching the 3D volumes of the broken parts, indicating that the rupture started within the specimen and grew to the circumference. This interpretation is supported by the fact that the XCT data did not reveal secondary macro-cracks at the surface of the specimens apart from the rupture itself.

Despite the fact that the initial voids could not be retraced in the broken specimens, we deduced from the shape of both the rupture area and of the initial voids that the initial void distribution did not cause the emergence of the intergranular cracks. Initial voids (due to manufacturing) do not seem to be the main contributor to creep failure in this PBF-LB/M/316L material. The analysis of metallographic sections of similarly produced creep specimens (see Ávila et al.^[11]) supports this conclusion. The final fracture is overall mainly intergranular. Our results differ from the results of Williams et al., who were able to attribute the emergence of cracks to the positions of the initial voids in their specimens.^[13] The shown results are in agreement with the work of Li et al., in spite of the different grain morphologies.^[14] The XCT and optical microscopy results show that the micro-cracks in the PBF-LB/M/316L creep specimens occur mainly at the grain boundaries that are oriented either 45° tilted to the loading direction, the theoretical region of maximum shear stress, or perpendicular to it. This differs slightly from the results of Williams et al. where creep cavities were observed at both grain boundaries oriented perpendicular and nearly parallel to the building direction.^[13] The mismatch between different reports highlights the dependency of PBF-LB/M/316L material properties on their specific production process

parameters. In fact, Williams et al. had used a different scanning strategy, a chessboard scanning with a 67° rotation; furthermore, they used a different PBF-LB/M machine which works with a pulsed laser mode instead of the more common continuous wave mode.^[13] Their process parameters and system set-up resulted in a different microstructure, with a lower proportion of horizontal grain boundaries (perpendicular to the loading direction). Also, the initial porosity of their specimens (0.4%) was much larger compared to the porosity <0.01% of the specimens in this study. Aside from the total number of voids, the defect size and shape are important: Williams et al. observed sharp-edged lack-of-fusion voids (of the size of their material's grains and above); consequently, they observed cracks growing from these elongated voids.^[13] The average size of the spherical voids observed in the specimens of this study is about a third of the grain size (75 µm) (reported by Ávila et al.^[11]). Therefore, the initial porosity of the PBF-LB/M/316L material of this study did not contribute to creep damage.

The XCT results revealed that clusters of micro-cracks were formed throughout the cross-section of the specimens.

The combined application of higher testing temperature and smaller applied load, which resulted in a decrease of the creep rupture time of about 60 %, appears to strongly contribute to the formation and amount of developed damage in the presented creep-loaded PBF-LB/M/316L material. Furthermore, the observation that the spatial density of the micro-cracks increased toward the location of the fracture surface for both specimens, where the cross-sectional area is reduced, suggests that geometrically induced local higher stresses contribute as well to the formation of damage.

It should finally be mentioned that the anisotropy of the microstructure impacts the mechanical properties of this PBF-LB/M/316L. The loading axis of our creep specimens coincides with the build direction. Results from creep testing may vary for different loading axes (e.g., perpendicular to the build direction).

5. Summary and Conclusions

Two PBF-LB/M specimens of stainless steel AISI 316L were analyzed by XCT at three stages of creep testing (prior to the test, after interruption, and after failure). Although the position of the initial voids through the three stages of the creep test could not be tracked, it could be shown that the initial porosity did not influence the evolution of creep damage in the specimens. The main mechanism of the material's damage was the formation of micro-cracks at grain boundaries perpendicular to the load axis. These intergranular cracks were not observed at the interrupted stage either because they were below the resolution of the XCT or that they had not yet initiated. In the specimen tested at 650 °C, a dense network of micro-cracks was observed throughout the whole length of the specimen, whereas for the specimen tested at 600 °C the occurrence of micro-cracks was localized near the final rupture surface. The correlation between the number of micro-cracks and the observed elongation indicates that micro-cracking is the main contribution to the creep extension in this material. Damage could only be clearly observed after the tertiary stage of creep in the studied specimens.

In the studied PBF-LB/M/316L material of this study large micro-cracks arise from the coalescence of isolated internal

micro-cracks without any visible cracks at the surface. This means a PBF-LB/M/316L material could be damaged without cracks being visible at its surface. This result must be considered when choosing the appropriate nondestructive testing techniques for safety inspection of PBF-LB/M/316L components.

The present results are in line with some works, but somewhat different from other studies of creep damage in PBF-LB/M/316L. This apparent ambiguity emphasizes the influence of the process parameters on the material's microstructure and the associated failure mechanisms of PBF-LB/M/316L. The authors deduce that process parameter can be used to design a microstructure that is optimized for the expected loading conditions.

Acknowledgements

This work was funded by the BAM Focus Area Materials project AGIL "Microstructure Development in Additively Manufactured Metallic Components: from Powder to Mechanical Failure". The authors are thankful for the financial support and the fruitful cooperation with all partners. The authors also thank Ms. Sina Schriever (BAM div. 5.2) for performing the creep tests and Mr. Steffen Thärig (BAM div. 5.2) for the optical microscopy. Open Access funding enabled and organized by Projekt DEAL.

Conflict of Interest

The authors declare no conflict of interest.

Data Availability Statement

The data that support the findings of this study are available from the corresponding author upon reasonable request.

Keywords

additive manufacturing, aisi 316l, computed tomography, creep, laser powder bed fusion, microstructure, pbf-lb/m

Received: November 2, 2022

Revised: February 20, 2023

Published online:

- [1] S. Kundu, R. Jones, D. Peng, N. Matthews, A. Alankar, S. R. K. Raman, P. Huang, *Materials* **2020**, *13*, 1341.
- [2] ISO/ASTM52900-21, *Additive Manufacturing — General Principles — Fundamentals and Vocabulary*, ASTM International, West Conshohocken, PA **2022**
- [3] W. E. Frazier, *J. Mater. Eng. Perform.* **2014**, *23*, 1917.
- [4] A. Khorasani, I. Gibson, J. K. Veetil, A. H. Ghasemi, *Int. J. Adv. Manuf. Technol.* **2020**, *108*, 191.
- [5] A. Mitchell, *Mater. Sci. Eng. A* **1998**, *243*, 257.
- [6] P. Vichare, A. Nassehi, S. Kumar, S. T. Newman, *Rob. Comput. Integr. Manuf.* **2009**, *25*, 999.
- [7] C. Hodonou, M. Balazinski, M. Brochu, C. Mascle, *Int. J. Adv. Manuf. Technol.* **2019**, *103*, 1509.
- [8] R. Baldev, U. Kamachi Mudali, M. Vijayalakshmi, M. D. Mathew, A. K. Bhaduri, P. Chellapandi, S. Venugopal, C. S. Sundar, B. P. C. Rao, B. Venkatraman, *Adv. Mater. Res.* **2013**, *794*, 3.
- [9] N. Kawasaki, in *15th GIF-IAEA Interface Meeting Presentations*, International Atomic Energy Agency (IAEA), Nuclear Power Technology Development Section and INPRO Section, Vienna (Austria), 29–30 June **2021**.
- [10] W. Beard, R. Lancaster, J. Adams, D. Buller, in *30th Int. Solid Freeform Fabrication Symp.* 2019, Austin, TX **2019**.
- [11] L. A. Ávila Calderón, B. Rehmer, S. Schriever, A. Ulbricht, L. A. Jácome, K. Sommer, G. Mohr, B. Skrotzki, A. Evans, *Mater. Sci. Eng. A* **2022**, *830*, 152847.
- [12] K. B. Yoon, V. H. Dao, J. M. Yu, *Fatigue Fract. Eng. Mater. Struct.* **2020**, *43*, 2623.
- [13] R. J. Williams, J. Al-Lami, P. A. Hooper, M.-S. Pham, C. M. Davies, *Addit. Manuf.* **2021**, *37*, 101706.
- [14] M. Li, X. Zhang, W.-Y. Chen, T. S. Byun, *J. Nucl. Mater.* **2021**, *548*, 152847.
- [15] J. M. Yu, V. H. Dao, K. B. Yoon, *J. Mech. Sci. Technol.* **2020**, *34*, 3249.
- [16] P. Dong, F. Vecchiato, Z. Yang, P. A. Hooper, M. R. Wenman, *Addit. Manuf.* **2021**, *40*, 101902.
- [17] X. Wang, J. A. Muñoz-Lerma, O. Sánchez-Mata, M. A. Shandiz, M. Brochu, *Mater. Sci. Eng. A* **2018**, *736*, 27.
- [18] S. K. Kurtz, F. M. A. Carpay, *J. Appl. Phys.* **1980**, *51*, 5725.
- [19] G. Mohr, S. J. Altenburg, A. Ulbricht, P. Heinrich, D. Baum, C. Maierhofer, K. Hilgenberg, *Metals* **2020**, *10*, 103.
- [20] A. Charmi, R. Falkenberg, L. Ávila, G. Mohr, K. Sommer, A. Ulbricht, M. Sprengel, R. S. Neumann, B. Skrotzki, A. Evans, *Mater. Sci. Eng. A* **2021**, *799*, 140154.
- [21] 204:2019-04, I, *Metallic Materials - Uniaxial Creep Testing in Tension - Method of Test*, International Organization for Standardization, Switzerland **2019**.
- [22] A. Buades, B. Coll, J.-M. Morel, *Image Process. Line* **2011**, *1*, 208.
- [23] J. Darbon, A. Cunha, T. F. Chan, S. Osher, G. J. Jensen, in *2008 5th IEEE Int. Symp. on Biomedical Imaging: From Nano to Macro*, Paris, France, 14–17 May **2008**.
- [24] J. Schindelin, I. Arganda-Carreras, E. Frise, V. Kaynig, M. Longair, T. Pietzsch, S. Preibisch, C. Rueden, S. Saalfeld, B. Schmid, J. Y. Tinevez, D. J. White, V. Hartenstein, K. Eliceiri, P. Tomancak, A. Cardona, *Nat. Methods* **2012**, *9*, 676.
- [25] S. Berg, D. Kutra, T. Kroeger, C. N. Straehle, B. X. Kausler, C. Haubold, M. Schiegg, J. Ales, T. Beier, M. Rudy, K. Eren, J. I. Cervantes, B. Xu, F. Beuttenmueller, A. Wolny, C. Zhang, U. Koethe, F. A. Hamprecht, A. Kreshuk, *Nat. Methods* **2019**, *16*, 1226.
- [26] M. Li, W.-Y. Chen, X. Zhang, *J. Nucl. Mater.* **2022**, *559*, 153469.
- [27] S. Sanchez, G. Gaspard, C. J. Hyde, I. A. Ashcroft, G. A. Ravi, A. T. Clare, *Mater. Des.* **2021**, *204*, 109647.
- [28] Z. Xu, C. J. Hyde, C. Tuck, A. T. Clare, *J. Mater. Process. Technol.* **2018**, *256*, 13.
- [29] J. H. Driver, C. Gorlier, C. Belrami, P. Violan, C. Amzallag, *ASTM STP* **1988**, *942*, 438.
- [30] D. G. Morris, D. R. Harries, *Metal Sci.* **1978**, *12*, 532.